ACS APPLIED MATERIALS & INTERFACES

Research Article

Cite This: ACS Appl. Mater. Interfaces 2019, 11, 8051−8059

www.acsami.org

Super Large $Sn_{1-x}Se$ Single Crystals with Excellent Thermoelectric Performance

Min Jin,[*,†,‡,◆] Xiao-Lei Shi,[§,◆] Tianli Feng,[⊥,#] Weidi Liu,[§] Haifeng Feng,[▽] Sokrates T. Pantelides,[⊥,#] Jun Jiang,[‡] Yunxia Chen,[†] Yi Du,[▽] Jin Zou,[*,§,∥] and Zhi-Gang Chen[*,○,§]

[†]College of Materials, Shanghai Dianji University, Shanghai 201306, P R China

[‡]Ningbo Institute of Materials Technology and Engineering, Chinese Academy of Sciences, Ningbo 315201, P R China

[§]Materials Engineeringand [∥]Centre for Microscopy and Microanalysis University of Queensland, Brisbane, QLD 4072, Australia

[⊥]Department of Physics and Astronomy and Department of Electrical Engineering and Computer Science, Vanderbilt University, Nashville, Tennessee 37235, United States

[#]Center for Nanophase Materials Sciences (CNMS), Oak Ridge National Laboratory, Oak Ridge, Tennessee 37831, United States

[▽]Institute for Superconducting and Electronic Materials (ISEM), Australian Institute for Innovative Materials (AIIM), University of Wollongong, Wollongong, NSW 2500, Australia

[○]Centre for Future Materials, University of Southern Queensland, Springfield, QLD 4300, Australia

Supporting Information

ABSTRACT: SnSe single crystals have drawn extensive attention for their ultralow thermal conductivity and outstanding thermoelectric performance. Here, we report super large $Sn_{1-x}Se$ single crystals with excellent thermoelectric properties, fabricated via an advanced horizontal Bridgman technique with great yield and high reproducibility. The obtained single crystals have a super large size of ~70 × 50 × 15 mm with a considerable weight of 148 g, which leads to a record-high mass density of >6.1 g cm^{-3}. Extensive chemical characterization demonstrates that ~0.3% Sn vacancies are present, which results in a large concentration of holes, ~1.2×10^{19} cm^{-3}, and an enhanced power factor of ~6.1 $\mu W\ cm^{-1}\ K^{-2}$ at 793 K. Simultaneously, the Sn-vacancy-induced lattice distortions result in a low thermal conductivity of ~0.39 $W\ m^{-1}\ K^{-1}$ at 793 K, leading to a competitive ZT of ~1.24. This work demonstrates that large-size off-stoichiometric SnSe single crystals hold promise to achieve high thermoelectric performance.

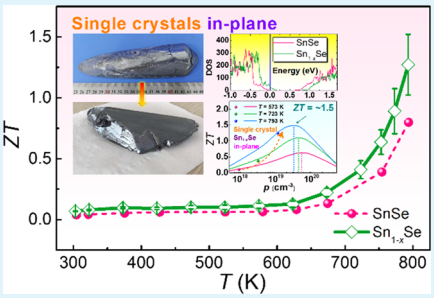

KEYWORDS: *Thermoelectric, Tin selenide, Single crystal, Characterizations, First-principles calculations*

1. INTRODUCTION

By offering a direct, quiet, and convenient conversion between electricity and thermal energy, thermoelectric materials are in principle able to provide a sustainable solution to the challenges of excessive energy consumption and environmental problems.[1−3] The efficiency of such direct energy conversion is evaluated by the dimensionless figure of merit $ZT = S^2\sigma T/\kappa$,[4] where σ, S, $S^2\sigma$, T, and κ are the electrical conductivity, Seebeck coefficient, power factor, absolute temperature, and thermal conductivity,[5,6] respectively. κ can be considered as the sum of κ_e and κ_l,[7] namely, the electronic and lattice contributions,[8] respectively. To achieve a high ZT, it is necessary to control the carrier concentration n to optimize the $S^2\sigma$.[9] At the same time, a low κ_l is essential.[10] To date, electron band structure and vibrational structure engineering have been two major strategies to achieve high $S^2\sigma$ and low κ_l.[11]

As a typical semiconductor with low cost, low toxicity, and low intrinsic κ, stannous selenide (SnSe) has received extensive attention because of its great potential to achieve high thermoelectric performance.[12] p-type SnSe single crystals have shown an ultrahigh ZT of ~2.6,[13] owing to their high $S^2\sigma$ and extremely low κ_l along the b-axis.[13,14] The advanced Bridgman technique can produce large-scale single crystals with a productivity of ~20 g each time[13] and large size of 13 × 15 mm.[15] However, the fabrication of SnSe single crystals is still complex and time-consuming to some extent,[16] and the thermoelectric performance below the phase-transition temperature (800 K) is still not excellent due to the low hole carrier concentration p of $<1 \times 10^{19}$ cm^{-3} at peak ZT for pure SnSe.[13] Besides, there are critical controversies on the reported ultralow κ in SnSe single crystals at high temperatures (<0.4 W m^{-1} K^{-1}).[17,18] To solve these issues, an improved crystal growth technique with a lower production cost and higher efficiency is required to realize large-size high-quality SnSe single-crystal production.

Received: December 12, 2018
Accepted: February 5, 2019
Published: February 5, 2019

DOI: 10.1021/acsami.8b21699
ACS Appl. Mater. Interfaces 2019, 11, 8051−8059

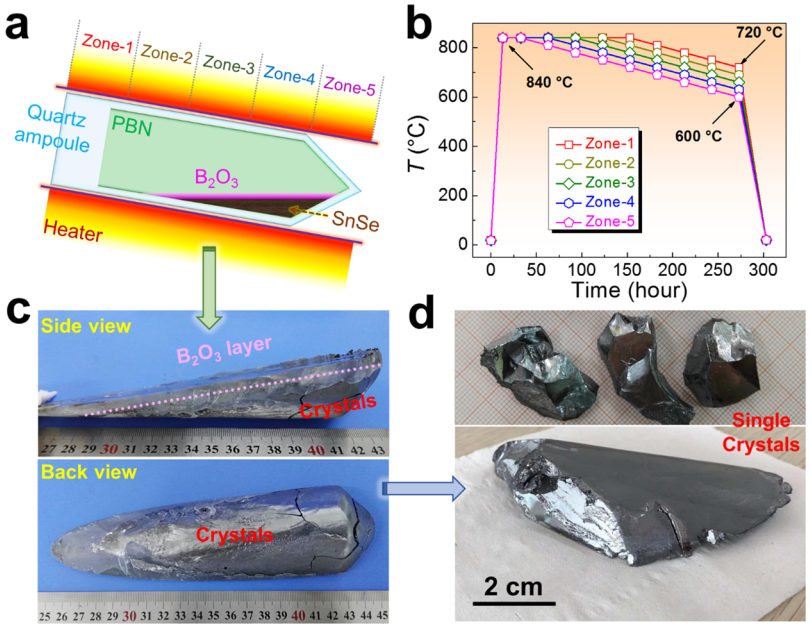

Figure 1. Fabrication of super large $Sn_{1-x}Se$ single crystals. (a) Illustration of the horizontal Bridgman (HB) method; (b) temperature program for $Sn_{1-x}Se$ single crystal growth; (c) side and back views of our synthesized $Sn_{1-x}Se$ single crystals before separation; (d) achieved $Sn_{1-x}Se$ single crystals.

Within the advanced crystal-growth techniques, the horizontal Bridgman (HB) method is a recently developed and promising crystal-growth route.[19] Compared to the vertical Bridgman (VB),[13] temperature gradient (TG),[20] and zone-melting (ZM)[21] methods, the HB technique can realize a much larger temperature gradient of ~3 K cm^{-1} and a higher cooling rate of ~25 K h^{-1},[19] enabling us to efficiently fabricate SnSe single crystals on a potentially industrial scale. Nevertheless, the achieved single crystals are still not large enough and exhibit microcracks.[19] Therefore, they cannot meet the requirement of fabricating thermoelectric devices and need further improvement. Meanwhile, for the strategies of further improving the thermoelectric performance of SnSe, previous studies indicate that inducing Sn vacancies in the SnSe matrix via off-stoichiometric design (such as $Sn_{0.98}Se$[9,22]) can effectively tune p to >1.2 × 10^{19} cm^{-3}, compared to ~6.7 × 10^{18} cm^{-3} in stoichiometric SnSe and realize enhanced ZTs to ~1.0 below 800 K in SnSe crystals.[9,23,24] In fact, the vacancies are inherent to SnSe and commonly observed in other chalcogenides and/or conventional thermoelectric materials such as Cu_2Se.[25,26]

In this work, we use an improved HB method to fabricate super large off-stoichiometric SnSe ($Sn_{1-x}Se$) single crystals with competitive high ZT of ~1.24 below the phase-transition temperature of 800 K. Figure 1a,b illustrates the crystal growth technique and the temperature program, respectively, in which we choose B_2O_3 as the encapsulant to prevent solution volatilization at high temperature[3] and use a highly elastic pyrolytic boron nitride (PBN) crucible as the lining to further eliminate thermal stress during the crystal-growth process in order to avoid microcracks in the fabricated single crystals. The achieved single crystal has a super large size of ~70 × 50 × 15 mm with a considerable weight of 148 g, which has a record-high mass density (>6.1 g cm^{-3}), as shown in Figure 1c,d. To realize off-stoichiometric SnSe single crystals grown by our improved HB method, we refer to the Sn−Se phase diagram (shown in Figure S1 in the Supporting Information) and adjust the stoichiometric ratio of precursors Sn and Se to be 0.98:1. Through detailed structural and compositional characterizations, including X-ray diffraction (XRD), X-ray photoelectron spectroscopy (XPS), energy dispersive spectroscopy (EDS), and electron probe microanalyzer (EPMA), we confirm that we realize off-stoichiometric SnSe single crystals. Compared with stoichiometric SnSe,[19] the Sn vacancy level of ~0.3% results in an improved p of ~1.2 × 10^{19} cm^{-3} at 793 K, as well as an enhanced $S^2\sigma$ of ~6.1 μW cm^{-1} K^{-2}. The higher Sn vacancy concentration observed in our samples explains why other SnSe single crystals obtained in the literature have different thermoelectric properties from ours.[19,27,28] In addition, our detailed structural and morphological characterizations using scanning electron microscopy (SEM), scanning tunneling microscopy (STM), transmission electron microscopy (TEM), and spherical aberration-corrected scanning TEM (Cs-STEM) confirm the single crystals and indicate that there are lattice distortions caused by Sn vacancies, which can effectively scatter the phonons and result in a low κ of ~0.39 W m^{-1} K^{-1} at 793 K, contributing to a competitive peak ZT of ~1.24 at this temperature.

2. EXPERIMENTAL SECTION

2.1. Reagents and Synthesis. SnSe single crystals were synthesized by using the HB method. High purity Sn (99.999%) and Se (99.999%) with a mole ratio of 0.98:1 were weighed as precursors (280 g in total). These precursors were loaded in a quartz ampoule (Ø 25 mm) and sealed by oxyhydrogen flame after the quartz ampoule was vacuumed to ~10^{-3} Pa. After that, the quartz ampoule was placed into a rocking furnace for synthesis. The furnace temperature was set at 930 °C to guarantee the full reaction of the precursors. After the solution was soaked for 30 min, the rocking system was rotated at a rate of 30 rpm for 0.5 h to ensure that the synthesis is homogeneous. Finally, the furnace was cooled to room temperature naturally, and SnSe polycrystals were obtained. These polycrystals were treated as the precursors of the followed single-crystal growth.

SnSe single-crystal growth was carried out in a HB furnace. The furnace was composed of five independent heating zones, as shown in

DOI: 10.1021/acsami.8b21699
ACS Appl. Mater. Interfaces 2019, 11, 8051−8059

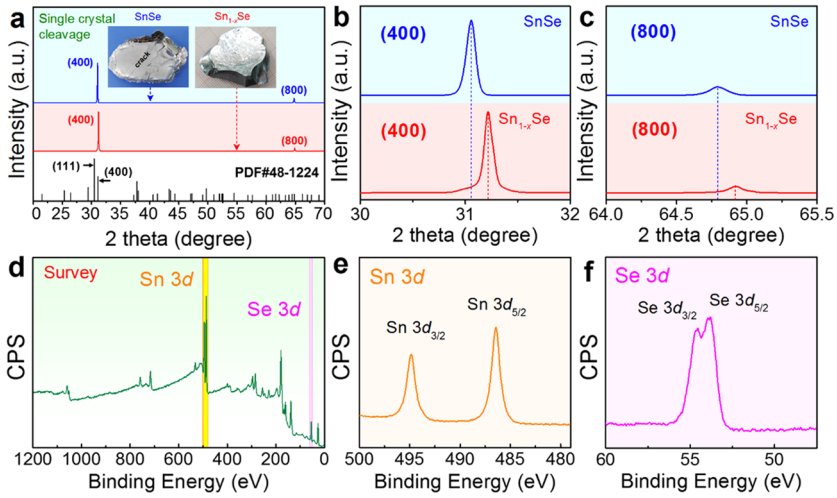

Figure 2. Structural characterizations of synthesized products. (a) XRD results for our SnSe and $Sn_{1-x}Se$ single crystals (on the cleavage surfaces); enlarged (b) 400* and (c) 800* peaks to see the peak deviation; (d) XPS spectrum of the survey scan for the $Sn_{1-x}Se$ single crystals (on the cleavage surfaces); high-resolution XPS scan for (e) Sn 3d and (f) Se 3d.

Figure 1a. The above synthesized polycrystalline SnSe together with the appropriate B_2O_3 encapsulant was loaded into a 5 N purity elastic pyrolytic boron nitride (PBN) crucible (Ø 55 mm with 0.8 mm in thickness), which was also sealed in a quartz ampoule with ~10^{-3} Pa vacuum. The B_2O_3 encapsulant would remain in solid state and float on the solution as its melting point is 450 °C and the density is only 2.46 g cm^{-3}. The quartz ampoule was moved into the HB furnace; its shoulder part was adjusted in the location corresponding to Zone 5. To achieve large-scale single crystals, the furnace tube was inclined ~30° to a horizontal plane so that most of the solution would stay on the corn part of the PBN crucible. Figure 1b shows the temperature program for SnSe single-crystal growth. Within 2 h, all the zones were heated to 840 °C, which was higher than the melting point of $SnSe_2$ but lower than that of SnSe, as shown in the Sn−Se phase diagram in Figure S1. After the solution was soaked for 35 h, crystal growth took place from Zone 5 to Zone 1 by decreasing the temperature gradually. The temperature gradient for SnSe crystal growth was about 2−3 °C cm^{-1}. As the temperatures of Zone 5 and Zone 1 were decreased to 600 and 720 °C, respectively, all the heating zones were cooled to room temperature simultaneously with a speed of ~30 °C h^{-1}. The as-grown single crystals were obtained by leaching the PBN crucible in ~50 °C carbinol (>99.7%) to dissolve B_2O_3.

2.2. Thermoelectric Property Measurements. The densities (ρ) of the single crystals were measured by the Archimedes method (DM50, China).[9] The achieved density of ~6.1 g cm^{-3} for $Sn_{1-x}Se$ is slightly lower than the theoretical values of 6.179 g cm^{-3} for SnSe and ~6.162 g cm^{-3} for $Sn_{1-x}Se$ (here, x = 0.003) due to the experimental error. In our measurements, σ and S were measured simultaneously using a Seebeck coefficient/electric resistivity measuring system (ZEM-3, ULVAC Technologies, Inc.) in the temperature range between 300 and 800 K. The thermal diffusivity D was measured using the laser flash diffusivity method (LFA 457, NETZSCH Group). κ was calculated using $\kappa = D \cdot C_p \cdot \rho$,[13] where C_p is the specific heat capacity obtained by differential scanning calorimetry (DSC 404 C; NETZSCH Group), and p was measured using the van der Pauw technique under a reversible magnetic field of 1.5 T. To ensure the repeatability of synthesized products and their demonstrated thermoelectric properties, each sample was measured at least three times.

2.3. Characterization. The synthesized single crystals were characterized by XRD (Bruker-D8) to determine their crystal structures by using Cu Kα radiation (λ = 1.5406 Å) at room temperature and XPS (Kratos Axis Ultra) to determine the Sn and Se valence states in SnSe. The morphological and chemical characteristics of single crystals were investigated using SEM (JSM-6610, JEOL Ltd.), and their structural characteristics were studied using HRTEM (TECNAI-F20) and Cs-corrected HR-STEM (Titan-G2). The TEM specimens of single crystals were prepared by focused ion beam technique (FEI Scios DualBeam System). EPMA (JEOL JXA-8200) was used to determine their compositions, and EDS (installed in TECNAI-F20) was used to identify the distribution of the elements. The instrumental error of EMPA is 0.1%. There were 50 test areas for each sample. The Sn vacancies were characterized by STM (STM1500, Unisoku Co.).

2.4. DFT Calculations. Density functional theory calculations were carried out using the Vienna ab initio simulation package (VASP)[29,30] with the projector augmented wave method (PAW)[30] and the generalized gradient approximation of Perdew−Burke−Ernzerhof (GGA-PBE)[31] for the electronic exchange-correlation functionals. The plane-wave energy cutoff was 450 eV. The SnSe unit cell was relaxed with a 6 × 18 × 18 Γ-centered k-mesh, and the convergence thresholds of the total energy and the forces on each atom were 10^{-8} eV and 10^{-6} eV $Å^{-1}$, respectively. The relaxed lattice constants are a = 11.7615 Å, b = 4.2062 Å, and c = 4.5475 Å. We constructed 2 × 4 × 4 (256 atoms) and 2 × 5 × 5 (400 atoms) supercells. The atoms in supercells were relaxed with 3 × 3 × 3 Γ-centered k-mesh until the forces of each atom were smaller than 10^{-3} eV $Å^{-1}$. The densities of states were calculated by using 3 × 3 × 3 Γ-centered k-mesh with the tetrahedron smearing method. The band structures along high-symmetry directions were calculated by using the Gaussian smearing method.

3. RESULTS AND DISCUSSION

3.1. Structural and Morphological Characteristics. To study the grown SnSe single crystals, we first investigated their structural and morphological characteristics. Figure 2a shows the XRD pattern of cleavage surfaces from the grown crystals (blue line for the stoichiometric SnSe and red line for the off-stoichiometric SnSe) with the inset showing optical images. The cleavage surfaces of synthesized single crystals show metallic luster. As shown in Figure 2a, only 400* and 800* diffraction peaks can be observed, which match the room-temperature α-SnSe phase by Standard Identification Card, JCPDS 48-1224, confirming that the SnSe single crystals are intrinsic and the cleavage surfaces are typical (100) surfaces.[9,12,16,24] No secondary phase is detectable, indicating that the single crystals have high purity. Figure 2b shows the magnified 400* diffraction peaks. Compared with stoichiometric SnSe, the 400* diffraction peak from the off-stoichiometric SnSe shifts toward higher angles (2θ),

DOI: 10.1021/acsami.8b21699
ACS Appl. Mater. Interfaces 2019, 11, 8051−8059

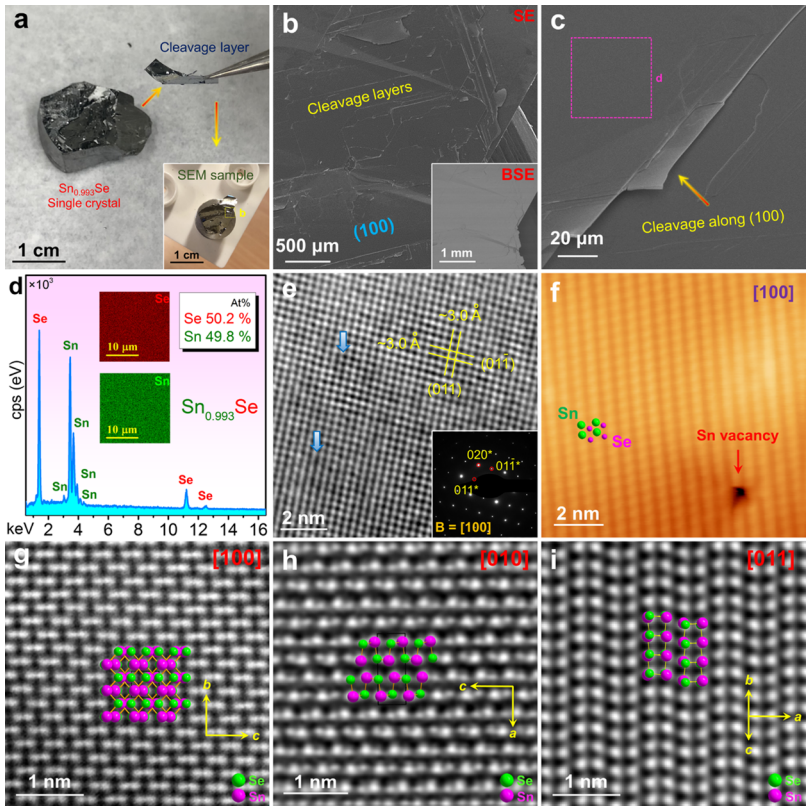

Figure 3. Morphological and compositional characterization of the $Sn_{1-x}Se$ single crystals. (a) SEM sample preparation for $Sn_{1-x}Se$ single crystal and the inset showing the top view of the sample on the holder; (b) SEM image of the $Sn_{1-x}Se$ cleavage surface taken from (a) to show the layered structure and the inset showing the back-scattering electron (BSE) image; (c) magnified SEM image to show the cleavage layers along (100); (d) EDS spot and map results taken from (c) to show the real composition of $Sn_{1-x}Se$; (e) HRTEM image of the $Sn_{1-x}Se$ cleavage surface to see the lattice distortions as the arrows indicate with the inset of the corresponding SAED pattern; (f) STM image of the $Sn_{1-x}Se$ cleavage surface to see a typical Sn vacancy; Cs-STEM images of $Sn_{1-x}Se$ taken along the (g) [100], (h) [010], and (i) [011] directions.

indicating a reduced lattice parameter *a*,[9,16,32] which is caused by the Sn vacancies.[9] To verify the Sn vacancies, we conduct statistical EDS and EPMA analysis, and the results indicate that the off-stoichiometric SnSe has an average Sn vacancy concentration of ~0.3%, that is, its composition is $Sn_{0.997}Se$. Figure 2c shows the magnified 800* diffraction peaks and exhibits similar results. In fact, according to the crystal-growth theory,[33] the crystal surfaces with a slow growth rate [such as (100)] prior to appearance in real crystals, and this is why the (100) surfaces are finally exposed in our super large SnSe single crystals. A previous study also reported that, compared with (010) and (011) surfaces, the (100) surfaces have the lowest surface energy,[34] indicating that (100) surfaces are much easier to form in real single crystals. Further discussion can be found in Section S2 in the Supporting Information.

Because the synthesized $Sn_{1-x}Se$ single crystals result from the selected ratio of precursors Sn and Se (0.98:1), to confirm the valence states of Sn and Se in our single crystals, we performed XPS analysis. Figure 2d shows the XPS scan in the entire binding energy range, indicating that except for Sn 3d and Se 3d energy states, there is no energy state from other elements (except C and O). Figure 2e,f also shows high-resolution XPS scans for Sn 3d and Se 3d, respectively, in which both Sn and Se exhibit only one valence state (Sn^{2+} for Sn and Se^{2-} for Se), indicating high purity of the SnSe phase.[35] The quantified atomic weights of Sn and Se are fitted well with the obtained ~0.3% of Sn vacancies.

Figure 3a shows a small piece of SnSe tissue cleaved by a sharp tweezer, which is used for the structural and morphological characterization. Figure 3b is a SEM image taken from the cleaved piece of the $Sn_{1-x}Se$ single crystal (enlarged from the inset of Figure 3a), in which the cleaved (100) surface of the intrinsic $Sn_{1-x}Se$ single crystal can be seen. The inset of Figure 3b shows the corresponding back-scattering electron (BSE) image, confirming that there is no compositional segregation of either Sn or Se on the microscale. Figure 3c is an enlarged SEM image, clearly showing that the SnSe layers are cleaved along (100) planes. All these results explain why there are only 400* and 800* peaks appearing in the XRD results taken from the cleavage surfaces. Figure 3d shows the EDS results of the single crystals. The spots were taken from 50 different sites, and the maps were taken from Figure 3c, indicating that both Sn and Se are homogeneously distributed. Figure 3e shows a high-resolution TEM (HRTEM) image, showing slight lattice distortions (as the arrows indicate), which are caused by the Sn vacancies.[3] The inset of Figure 3e shows the corresponding selected area electron diffraction (SAED) pattern indexed as a typical *α*-SnSe phase with a (100) surface.[9,12] Figure 3f is a high-resolution STM image, showing a typical Sn vacancy.[20,36,37] Figure 3g–i shows STEM high-angle annular dark field (HAADF) images taken along the [100], [010], and [011] directions, respectively. The overlays in the normal areas show Se atoms in green and Sn atoms in purple, all indicating the typical orthorhombic *α*-SnSe phase.

DOI: 10.1021/acsami.8b21699
ACS Appl. Mater. Interfaces 2019, 11, 8051–8059

3.2. Thermoelectric Performance. To evaluate their thermoelectric performance, we cut and polished the synthesized $Sn_{1-x}Se$ single crystals into regular shapes, as shown in the inset of Figure 4. We chose three different

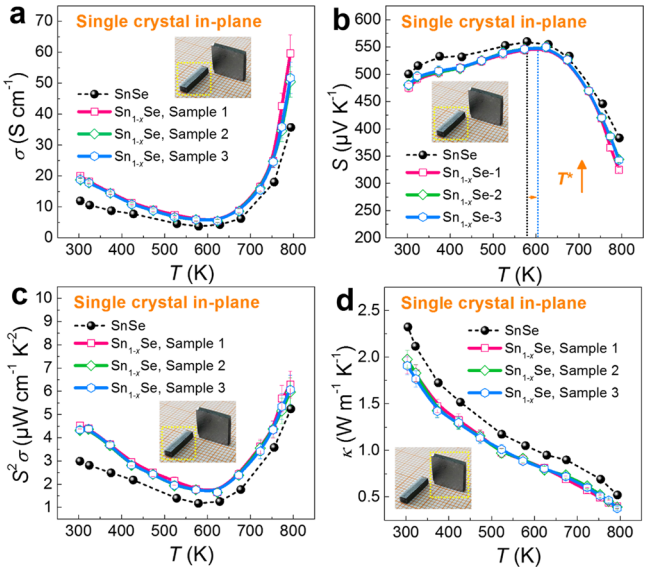

Figure 4. Plots of measured T-dependent properties from SnSe and $Sn_{1-x}Se$ single crystals along the in-plane direction (bc-axis): (a) σ; (b) S; (c) $S^2\sigma$; (d) κ.

$Sn_{1-x}Se$ single-crystal samples to investigate their performance stabilities. The stoichiometric SnSe single-crystal sample was also investigated for comparison.[19] Since Se can volatilize from SnSe at high temperatures[3] [see our measured thermogravimetric (TG) results shown in Figure S3] and since the phase transition may induce microcracks in the SnSe matrix, we selected the measured temperature range to be 300−793 K. High repeatability was realized with measured fluctuations being 10, 2, and 5% for σ, S, and κ, respectively, as shown in Figure S4. Besides, for p-type SnSe, considering that all properties except S measured along the bc-axis (in-plane) are higher than that measured along the a-axis (out-of-plane) due to the anisotropy (shown in Figure S5 in the Supporting Information),[9,13,38] we chose the bc-axis as the main measured direction in the following discussion. Figure 4a shows the temperature-dependent σ. Compared with stoichiometric SnSe, the σ values obtained from $Sn_{1-x}Se$ single crystals are significantly improved, especially at high temperature (>750 K) due to the higher Sn vacancy concentration, which releases more holes via thermal activation.[3] Figure 4b exhibits the temperature-dependent S, showing that the S values of $Sn_{1-x}Se$ single crystals drop significantly at high temperatures (>650 K), indicating an increase of p,[3,9] fitting well with the results of σ. Peak S values can be achieved at the bipolar-effect temperature T^*, and a shifting of T^* toward a higher T for $Sn_{1-x}Se$ also indicates an increase of p.[3,9] Figure 4c shows the determined $S^2\sigma$, from which a high average $S^2\sigma$ of 6.06 μW cm^{-1} K^{-2} at 793 K can be secured in the $Sn_{1-x}Se$ single crystals. Figure 4d plots the calculated T-dependent κ via κ =

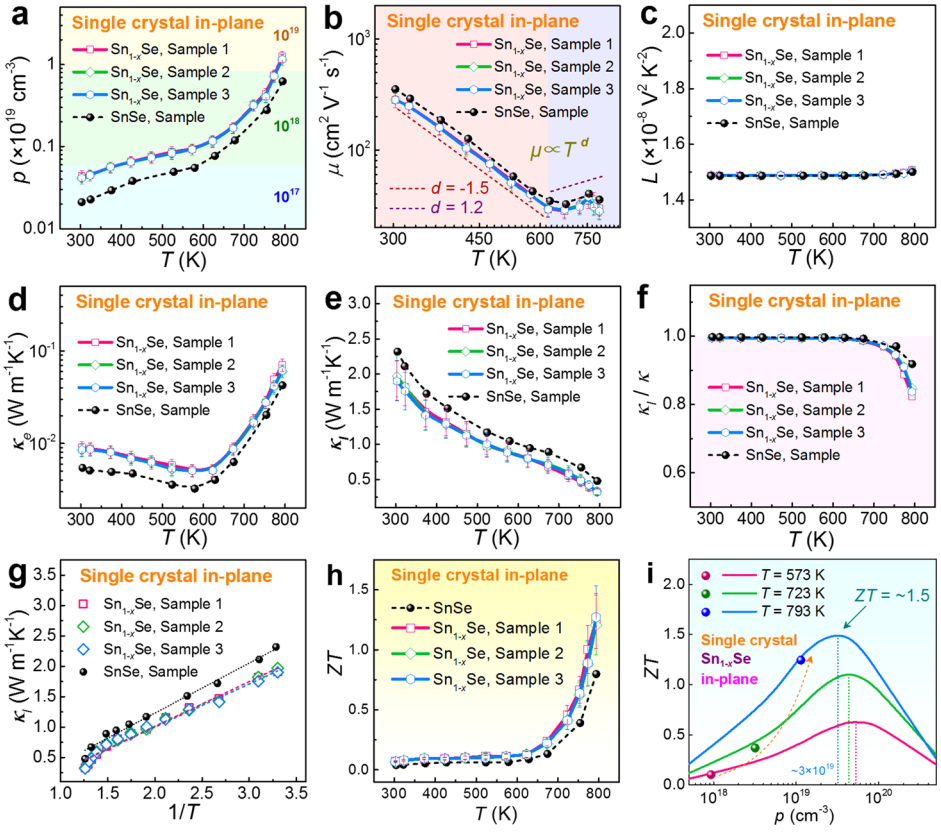

Figure 5. Extended thermoelectric properties for SnSe single crystals along the in-plane direction (bc-axis): T-dependent (a) p; (b) μ; (c) L; (d) κ_e; (e) κ_l; T-dependent (f) κ_l/κ ratio; (g) $1/T$-dependent κ_l; (h) ZT compared with stoichiometric SnSe; (i) comparison of achieved ZTs with predicted ZTs.

DOI: 10.1021/acsami.8b21699
ACS Appl. Mater. Interfaces 2019, 11, 8051−8059

$D \cdot C_p \cdot \rho$,[9] where the measured D and ρ values are plotted in Figure S6a, and the measured C_p is shown in Figure S6b. As can be seen, compared with stoichiometric SnSe, κ values of $Sn_{1-x}Se$ single crystals are significantly decreased from room temperature to 793 K. This is because the induced Sn vacancies and thus the slightly distorted lattice can effectively scatter the phonons from short and medium wavelengths.[3,12,16,24] An extra low κ of ~0.39 W m^{-1} K^{-1} is achieved at 793 K, which is close to the results from a previous study (~0.4 W m^{-1} K^{-1} at 773 K).[13] Besides, considering the high relative densities in the single crystals (all > 98.7%),[13,17] the obtained κ values must be intrinsic.

To confirm the improved p at high temperature, we measured the temperature-dependent p, as shown in Figure 5a. As can be seen, the $Sn_{1-x}Se$ has higher p than SnSe due to the extra holes provided by the Sn vacancies. The p of $Sn_{1-x}Se$ at 793 K can reach >1 × 10^{19} cm^{-3} triggered by thermal activation, and the induced ~0.3% Sn vacancies play a significant role in producing more holes under thermal excitation, contributing to such high p values.[3] To better understand the carrier transport principles, Figure 5b plots the corresponding carrier mobility μ, which roughly follows the power law ($\mu \propto T^d$).[27,35] It is seen that, from room temperature to ~623 K, μ decreases roughly following $\mu \propto T^{-1.5}$, indicating that acoustic-phonon scattering dominates carrier scattering.[27,35] However, from ~623 to ~750 K, there is an increase of μ roughly following $\mu \propto T^{1.2}$, which should be derived from thermal excitation near the phase transition.[10] Meanwhile, $Sn_{1-x}Se$ single crystals possess lower μ than SnSe for the entire temperature range due to the crystal imperfections (mainly Sn vacancies and lattice distortions) in $Sn_{1-x}Se$, which block and/or scatter carriers and in turn impede the carrier transportation. Besides, as shown in Figure S5, the p is weakly dependent on the measured direction, but the μ is strongly dependent on it, from which the μ along the out-of-plane is significantly lower than that along the in-plane, which is derived from the strong anisotropy of SnSe.[9,12,13,16,24]

From Figure 4d, an obvious reduction of κ from 600 to 800 K can be observed, even though there is a minor carrier activation at this temperature as shown in Figure 5a, which should result in an increase of κ due to the increase of κ_e. In fact, previous works also reported similar results on single-crystal SnSe—the κ continued to reduce from 600 to 800 K until the phase transition at 800 K.[13−15,20,39] To further understand such unusual behavior, we study the contributions from electrons and lattice on the κ, and the κ_e is calculated via the Wiedemann−Franz law $\kappa_e = L \cdot \sigma \cdot T$,[3,40] where L is the Lorenz number calculated from the single parabolic band (SPB) model[25,26,41,42] as shown in Figure 5c. The calculation details can be found in Section S7 in the Supporting Information. For L, the value is relatively constant at ~1.5 × 10^{-8} V^2 K^{-2} in the entire temperature range.[24] Figure 5d,e shows the calculated temperature-dependent κ_e and κ_l, respectively, and κ_l is obtained by subtracting the electronic contribution κ_e from κ. We find that the electron contribution is much lower than the lattice contribution, and the latter takes about 82% of the total κ as shown in Figure 5f. We find that the κ_l shows a slower scaling with temperature (from 300 to 600 K) than the $1/T$ trend induced by phonon−phonon scattering, as shown in Figure 5g. This indicates the existence of considerable phonon-defect scattering with Sn vacancies and concomitant lattice distortions in $Sn_{1-x}Se$, which lead to low κ_l. With the temperatures above 600 K, the crystals are approaching to the phase transition regime and the κ_l goes below 0.33 W m^{-1} K^{-1} at 793 K. It should be noted that this value is close to the minimum κ_l (0.33 W m^{-1} K^{-1} along the c-axis and 0.36 W m^{-1} K^{-1} along the b-axis[13,43]) calculated via a classical Debye−Cahill model.[44]

Figure 5h exhibits the T-dependent ZTs with a high peak ZT of ~1.24 at 793 K observed before the phase transition, indicating that $Sn_{1-x}Se$ possesses considerable potential for thermoelectric applications.[1,3] Figure 5i compares the measured ZT values with the predicted ones from the SPB model at different temperatures.[41,42,45,46] We find that the experimental p values are all located below the theoretical optimal values. Therefore, increasing p is key to improving the thermoelectric performance. In this work, the achieved high p of ~1.2 × 10^{19} cm^{-3} induced by the large Sn vacancy concentration is fairly close to the optimal value of 3 × 10^{19} cm^{-3} at 793 K, which partially explains the achieved high ZT of ~1.24. In the future, higher ZTs may be achieved by further increasing p. Besides, it should be noticed that the ZT value achieved at this temperature (close to phase transition) may be slightly overestimated. This is because the C_p was measured using high-temperature differential scanning calorimetry. For SnSe, which is a typical anharmonic material,[3,47−49] the discrepancy between constant-pressure specific heat C_p and constant-volume specific heat C_v is offset to the first order by a decrease in the packing density due to thermal expansion. However, this is not accurate near the phase transition temperature. Hence, it can be assumed that C_p equals C_v at all temperatures, except at phase transition temperature. Considering these, this ZT value near the phase transition may be overestimated due to the total κ derived from the measured C_p.

3.3. First-Principles Studies. To further understand the mechanism of the increase of p, we conducted density functional theory (DFT) calculations of the electronic band structures of SnSe and $Sn_{1-x}Se$, as shown in Figure 6a,b, respectively. For SnSe and $Sn_{1-x}Se$, we used $Sn_{128}Se_{128}$ and $Sn_{127}Se_{128}$ stoichiometries, respectively, by using 2 × 4 × 4 (256 atoms) supercells. It is clear that the Fermi level moves

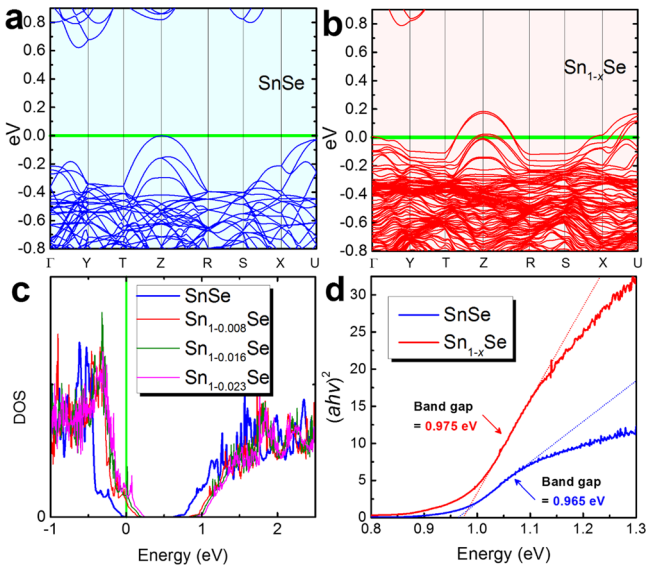

Figure 6. Comparisons of calculated band structures for (a) SnSe and (b) $Sn_{1-x}Se$; comparisons of (c) DOS and (d) measured band gap values of SnSe and $Sn_{1-x}Se$.

DOI: 10.1021/acsami.8b21699
ACS Appl. Mater. Interfaces 2019, 11, 8051−8059

into the valence band with the presence of a Sn vacancy in the supercell, indicating that the Sn vacancy changes SnSe into a degenerate p-type semiconductor with significantly increased p. To further unveil the impact of increasing the Sn vacancy concentration, we also calculated the electronic band structures of $Sn_{126}Se_{128}$ and $Sn_{125}Se_{128}$ (with two and three Sn vacancies in the supercell, respectively). The densities of states (DOS) of $Sn_{128}Se_{128}$, $Sn_{127}Se_{128}$, $Sn_{126}Se_{128}$, and $Sn_{125}Se_{128}$ are compared in Figure 6c, in which it is seen that the Fermi level moves more deeply into the valence band with increasing Sn vacancies. Therefore, the calculations clearly demonstrate that the Sn vacancies contribute to the increased p and in turn an enhanced $S^2\sigma$, agreeing with the experimental results shown in Figure 4.[50−52] Figure 6d shows the measured band gaps of SnSe and $Sn_{1-x}Se$ at room temperature (α-SnSe), which shows that the band gap increases after introducing Sn vacancies but the increment is negligible (from ∼0.965 to ∼0.975 eV). Although DFT calculations are well known for the underestimation of band gaps,[53,54] we find that they predict the same trend as what we measured, that is, the band gap increases negligibly with increasing Sn vacancies. The measured band gap values are consistent with the previously reported values of ∼0.9 eV.[3] The calculated effective mass (m^*) value via the SPB model is ∼1.11m_0 (shown in Figure S7), which is also close to the previously reported values.[3,24] These results indicate that SnSe is a typical narrow-gap semiconductor with promising thermoelectric properties. The difference between the experimental and theoretical calculated p for $Sn_{1-x}Se$ can be seen in Figure S8.

Considering the significance of Sn vacancy on the enhancement of thermoelectric performance, there are some potential routes to further enhance the Sn vacancy concentration in the SnSe matrix, including adjusting the synthesis temperature and the synthesis time to alter the reaction kinetics and in turn produce more Sn vacancies,[3] which need further experiments to demonstrate. Meanwhile, there is also considerable potential to further improve the thermoelectric properties via proper band engineering such as doping.[3,39] Besides, it should be noticed that there could be mechanical stability issues for a device when employing single-crystal SnSe. Considering the changes in lattice parameters as a function of temperature near the displacive phase transition, especially arising from the negative thermal expansion along the c-axis, the phase transition may lead to electrical contact issues in the thermoelectric legs of the device itself. This is why we avoid measuring the thermoelectric properties over the phase transition temperature at 800 K.

4. CONCLUSIONS

In conclusion, we fabricated large-size off-stoichiometric SnSe single crystals with a Sn vacancy level of ∼0.3% via an improved horizontal Bridgman method for the first time. The grown single crystals have a super large size of ∼70 × 50 × 15 mm with a weight of 148 g and a record-high mass density of >6.1 g cm^{-3}. A competitive ZT of ∼1.24 is achieved at 793 K owing to the enhanced power factor and the reduced lattice thermal conductivity. This work provides a new perspective in achieving excellent thermoelectric properties of SnSe.

■ ASSOCIATED CONTENT

Supporting Information

The Supporting Information is available free of charge on the ACS Publications website at DOI: 10.1021/acsami.8b21699.

Sn−Se phase diagram, XRD and SEM results for polycrystalline SnSe, TG curves of products, reproducibility and anisotropy of thermoelectric performance, measured D and C_p, calculated m^* via the SPB model with detailed calculations, and calculated theoretical p via DFT (PDF).

■ AUTHOR INFORMATION

Corresponding Authors

*E-mail: jmaish@aliyun.com (M.J.).
*E-mail: j.zou@uq.edu.au (J.Z.).
*E-mail: zhigang.chen@usq.edu.au; zhigang.chen@uq.edu.au (Z.-G.C).

ORCID

Xiao-Lei Shi: 0000-0003-0905-2547
Tianli Feng: 0000-0002-7284-5657
Haifeng Feng: 0000-0002-6890-161X
Jin Zou: 0000-0001-9435-8043
Zhi-Gang Chen: 0000-0002-9309-7993

Author Contributions

◆M.J. and X.-L.S. contributed equally to this work.

Notes

The authors declare no competing financial interest.

■ ACKNOWLEDGMENTS

This work is financially supported by the Public Projects of Zhejiang Province (2017C31006), the National Natural Science Foundation of China (Grant No. 51809161), the Shanghai Municipal Natural Science Foundation (Grant No.18ZR1416000), and the Australian Research Council. X.-L.S. thanks the IPRS for providing his PhD program. We acknowledge YZ and LSQ for Hall measurement and ZWC for discussion. The Australian Microscopy & Microanalysis Research Facility is acknowledged for providing characterization facilities. Theoretical work by T.F. and S.T.P. is supported in part by the Department of Energy grant DE-FG0209ER46554 and by the McMinn Endowment. Computations at Vanderbilt University and ORNL were performed at the National Energy Research Scientific Computing Center (NERSC), a Department of Energy, Office of Science, User Facility funded through Contract No. DE-AC02-05CH11231. Computations also used the Extreme Science and Engineering Discovery Environment (XSEDE).

■ REFERENCES

(1) Zhu, T.; Liu, Y.; Fu, C.; Heremans, J. P.; Snyder, J. G.; Zhao, X. Compromise and Synergy in High-Efficiency Thermoelectric Materials. *Adv. Mater.* **2017**, *29*, 1605884.

(2) Zhao, L.-D.; Dravid, V. P.; Kanatzidis, M. G. The Panoscopic Approach to High Performance Thermoelectrics. *Energy Environ. Sci.* **2014**, *7*, 251−268.

(3) Chen, Z.-G.; Shi, X.; Zhao, L.-D.; Zou, J. High-Performance SnSe Thermoelectric Materials: Progress and Future Challenge. *Prog. Mater. Sci.* **2018**, *97*, 283−346.

(4) Yang, L.; Chen, Z.-G.; Dargusch, M. S.; Zou, J. High Performance Thermoelectric Materials: Progress and Their Applications. *Adv. Energy Mater.* **2018**, *8*, 1701797.

(5) Zhao, K.; Duan, H.; Raghavendra, N.; Qiu, P.; Zeng, Y.; Zhang, W.; Yang, J.; Shi, X.; Chen, L. Solid-State Explosive Reaction for Nanoporous Bulk Thermoelectric Materials. *Adv. Mater.* **2017**, *29*, 1701148.

(6) Dresselhaus, M. S.; Chen, G.; Tang, M. Y.; Yang, R. G.; Lee, H.; Wang, D. Z.; Ren, Z. F.; Fleurial, J.-P.; Gogna, P. New Directions for

DOI: 10.1021/acsami.8b21699
ACS Appl. Mater. Interfaces 2019, 11, 8051−8059

Low-Dimensional Thermoelectric Materials. *Adv. Mater.* **2007**, *19*, 1043−1053.
(7) Moshwan, R.; Yang, L.; Zou, J.; Chen, Z.-G. Eco-friendly SnTe Thermoelectric Materials: Progress and Future Challenges. *Adv. Funct. Mater.* **2017**, *27*, 1703278.
(8) Liu, W.-D.; Chen, Z.-G.; Zou, J. Eco-Friendly Higher Manganese Silicide Thermoelectric Materials: Progress and Future Challenges. *Adv. Energy Mater.* **2018**, 1800056.
(9) Shi, X.; Chen, Z.-G.; Liu, W.; Yang, L.; Hong, M.; Moshwan, R.; Huang, L.; Zou, J. Achieving High Figure of Merit in *p*-Type Polycrystalline $Sn_{0.98}Se$ *via* Self-Doping and Anisotropy-Strengthening. *Energy Storage Mater.* **2018**, *10*, 130−138.
(10) Jin, M.; Chen, Z.; Tan, X.; Shao, H.; Liu, G.; Hu, H.; Xu, J.; Yu, B.; Shen, H.; Xu, J.; Jiang, H.; Pei, Y.; Jiang, J. Charge Transport in Thermoelectric SnSe Single Crystals. *ACS Energy Lett.* **2018**, *3*, 689−694.
(11) Chen, Z.-G.; Han, G.; Yang, L.; Cheng, L.; Zou, J. Nanostructured Thermoelectric Materials: Current Research and Future Challenge. *Prog. Nat. Sci.* **2012**, *22*, 535−549.
(12) Shi, X.-L.; Zheng, K.; Liu, W.-D.; Wang, Y.; Yang, Y.-Z.; Chen, Z.-G.; Zou, J. Realizing High Thermoelectric Performance in *n*-Type Highly Distorted Sb-Doped SnSe Microplates *via* Tuning High Electron Concentration and Inducing Intensive Crystal Defects. *Adv. Energy Mater.* **2018**, *8*, 1800775.
(13) Zhao, L.-D.; Lo, S.-H.; Zhang, Y.; Sun, H.; Tan, G.; Uher, C.; Wolverton, C.; Dravid, V. P.; Kanatzidis, M. G. Ultralow Thermal Conductivity and High Thermoelectric Figure of Merit in SnSe Crystals. *Nature* **2014**, *508*, 373−377.
(14) Chang, C.; Wu, M.; He, D.; Pei, Y.; Wu, C.-F.; Wu, X.; Yu, H.; Zhu, F.; Wang, K.; Chen, Y.; Huang, L.; Li, J.-F.; He, J.; Zhao, L.-D. 3D Charge and 2D Phonon Transports Leading to High Out-of-Plane *ZT* in *n*-Type SnSe Crystals. *Science* **2018**, *360*, 778−783.
(15) Peng, K.; Lu, X.; Zhan, H.; Hui, S.; Tang, X.; Wang, G.; Dai, J.; Uher, C.; Wang, G.; Zhou, X. Broad Temperature Plateau for High *ZT*s in Heavily Doped *p*-Type SnSe Single Crystals. *Energy Environ. Sci.* **2016**, *9*, 454−460.
(16) Shi, X.; Zheng, K.; Hong, M.; Liu, W.; Moshwan, R.; Wang, Y.; Qu, X.; Chen, Z.-G.; Zou, J. Boosting the Thermoelectric Performance of *p*-Type Heavily Cu-doped Polycrystalline SnSe *via* Inducing Intensive Crystal Imperfections and Defect Phonon Scattering. *Chem. Sci.* **2018**, *9*, 7376−7389.
(17) Wei, P.-C.; Bhattacharya, S.; He, J.; Neeleshwar, S.; Podila, R.; Chen, Y. Y.; Rao, A. M. The Intrinsic Thermal Conductivity of SnSe. *Nature* **2016**, *539*, E1−E2.
(18) Ibrahim, D.; Vaney, J.-B.; Sassi, S.; Candolfi, C.; Ohorodniichuk, V.; Levinsky, P.; Semprimoschnig, C.; Dauscher, A.; Lenoir, B. Reinvestigation of the Thermal Properties of Single-Crystalline SnSe. *Appl. Phys. Lett.* **2017**, *110*, 032103.
(19) Jin, M.; Shao, H.; Hu, H.; Li, D.; Shen, H.; Xu, J.; Jiang, J. Growth and Characterization of Large Size Undoped *p*-Type SnSe Single Crystal by Horizontal Bridgman Method. *J. Alloys Compd.* **2017**, *712*, 857−862.
(20) Duong, A. T.; Nguyen, V. Q.; Duvjir, G.; Duong, V. T.; Kwon, S.; Song, J. Y.; Lee, J. K.; Lee, J. E.; Park, S.; Min, T.; Lee, J.; Kim, J.; Cho, S. Achieving *ZT* = 2.2 with Bi-doped *n*-Type SnSe Single Crystals. *Nat. Commun.* **2016**, *7*, 13713.
(21) He, J.; Tan, X.; Xu, J.; Liu, G.-Q.; Shao, H.; Fu, Y.; Wang, X.; Liu, Z.; Xu, J.; Jiang, H.; Jiang, J. Valence Band Engineering and Thermoelectric Performance Optimization in SnTe by Mn-Alloying *via* a Zone-Melting Method. *J. Mater. Chem. A* **2015**, *3*, 19974−19979.
(22) Sist, M.; Zhang, J.; Brummerstedt Iversen, B. Crystal Structure and Phase Transition of Thermoelectric SnSe. *Acta Crystallogr. B* **2016**, *72*, 310−316.
(23) Wei, W.; Chang, C.; Yang, T.; Liu, J.; Tang, H.; Zhang, J.; Li, Y.; Xu, F.; Zhang, Z.; Li, J.-F.; Tang, G. Achieving High Thermoelectric Figure of Merit in Polycrystalline SnSe *via* Introducing Sn Vacancies. *J. Am. Chem. Soc.* **2017**, *140*, 499−505.
(24) Shi, X.; Wu, A.; Liu, W.; Moshwan, R.; Wang, Y.; Chen, Z.-G.; Zou, J. Polycrystalline SnSe with Extraordinary Thermoelectric Property *via* Nanoporous Design. *ACS Nano* **2018**, *12*, 11417−11425.
(25) Liu, W.; Shi, X.; Hong, M.; Yang, L.; Moshwan, R.; Chen, Z.-G.; Zou, J. Ag Doping Induced Abnormal Lattice Thermal Conductivity in Cu_2Se. *J. Mater. Chem. C* **2018**, *6*, 13225−13231.
(26) Liu, W.; Shi, X.; Moshwan, R.; Hong, M.; Yang, L.; Chen, Z.-G.; Zou, J. Enhancing Thermoelectric Performance of $(Cu_{1-x}Ag_x)_2Se$ *via* CuAgSe Secondary Phase and Porous Design. *Sustainable Mater. Technol.* **2018**, *17*, No. e00076.
(27) Nassary, M. The Electrical Conduction Mechanisms and Thermoelectric Power of SnSe Single Crystals. *Turk. J. Phys.* **2009**, *33*, 201−208.
(28) Wang, S.; Hui, S.; Peng, K.; Bailey, T. P.; Liu, W.; Yan, Y.; Zhou, X.; Tang, X.; Uher, C. Low Temperature Thermoelectric Properties of *p*-Type Doped Single-Crystalline SnSe. *Appl. Phys. Lett.* **2018**, *112*, 142102.
(29) Kresse, G.; Hafner, J. *Ab initio* Molecular Dynamics for Liquid Metals. *Phys. Rev. B* **1993**, *47*, 558.
(30) Kresse, G.; Furthmüller, J. Efficient Iterative Schemes for *ab initio* Total-Energy Calculations Using a Plane-Wave Basis Set. *Phys. Rev. B* **1996**, *54*, 11169.
(31) Perdew, J. P.; Burke, K.; Ernzerhof, M. Generalized Gradient Approximation Made Simple. *Phys. Rev. Lett.* **1996**, *77*, 3865.
(32) Gao, J.; Zhu, H.; Mao, T.; Zhang, L.; Di, J.; Xu, G. The Effect of Sm Doping on the Transport and Thermoelectric Properties of SnSe. *Mater. Res. Bull.* **2017**, *93*, 366−372.
(33) Jin, M.; Shao, H.; Hu, H.; Li, D.; Xu, J.; Liu, G.; Shen, H.; Xu, J.; Jiang, H.; Jiang, J. Single Crystal Growth of $Sn_{0.97}Ag_{0.03}Se$ by a Novel Horizontal Bridgman Method and its Thermoelectric Properties. *J. Cryst. Growth* **2017**, *460*, 112−116.
(34) Ma, X.-H.; Cho, K.-H.; Sung, Y.-M. Growth Mechanism of Vertically Aligned SnSe Nanosheets *via* Physical Vapour Deposition. *CrystEngComm* **2014**, *16*, 5080−5086.
(35) Li, Y.; Li, F.; Dong, J.; Ge, Z.; Kang, F.; He, J.; Du, H.; Li, B.; Li, J.-F. Enhanced Mid-Temperature Thermoelectric Performance of Textured SnSe Polycrystals Made of Solvothermally Synthesized Powders. *J. Mater. Chem. C* **2016**, *4*, 2047−2055.
(36) Kim, S.-u.; Duong, A.-T.; Cho, S.; Rhim, S. H.; Kim, J. A Microscopic Study Investigating the Structure of SnSe Surfaces. *Surf. Sci.* **2016**, *651*, 5−9.
(37) Duvjir, G.; Min, T.; Thi Ly, T.; Kim, T.; Duong, A.-T.; Cho, S.; Rhim, S. H.; Lee, J.; Kim, J. Origin of *p*-Type Characteristics in a SnSe Single Crystal. *Appl. Phys. Lett.* **2017**, *110*, 262106.
(38) Chang, C.; Zhao, L.-D. Anharmoncity and Low Thermal Conductivity in Thermoelectrics. *Mater. Today Phys.* **2018**, *4*, 50−57.
(39) Zhao, L.-D.; Tan, G.; Hao, S.; He, J.; Pei, Y.; Chi, H.; Wang, H.; Gong, S.; Xu, H.; Dravid, V. P.; Uher, C.; Snyder, G. J.; Wolverton, C.; Kanatzidis, M. G. Ultrahigh Power Factor and Thermoelectric Performance in Hole-Doped Single-Crystal SnSe. *Science* **2016**, *351*, 141−144.
(40) Moshwan, R.; Shi, X.-L.; Liu, W.-D.; Yang, L.; Wang, Y.; Hong, M.; Auchterlonie, G.; Zou, J.; Chen, Z.-G. High Thermoelectric Performance in Sintered Octahedron-Shaped $Sn(CdIn)_xTe_{1+2x}$ Microcrystals. *ACS Appl. Mater. Interfaces* **2018**, *10*, 38944−38952.
(41) Xu, Y.; Li, W.; Wang, C.; Li, J.; Chen, Z.; Lin, S.; Chen, Y.; Pei, Y. Performance Optimization and Single Parabolic Band Behavior of Thermoelectric MnTe. *J. Mater. Chem. A* **2017**, *5*, 19143−19150.
(42) Shen, J.; Chen, Z.; lin, S.; Zheng, L.; Li, W.; Pei, Y. Single Parabolic Band Behavior of Thermoelectric *p*-Type CuGaTe2. *J. Mater. Chem. C* **2016**, *4*, 209−214.
(43) Yang, J.; Zhang, G.; Yang, G.; Wang, C.; Wang, Y. X. Outstanding Thermoelectric Performances for both *p*- and *n*-Type SnSe from First-Principles Study. *J. Alloys Compd.* **2015**, *644*, 615−620.
(44) Cahill, D. G.; Watson, S. K.; Pohl, R. O. Lower Limit to the Thermal Conductivity of Disordered Crystals. *Phys. Rev. B* **1992**, *46*, 6131.

DOI: 10.1021/acsami.8b21699
ACS Appl. Mater. Interfaces 2019, 11, 8051−8059

(45) She, X.; Su, X.; Du, H.; Liang, T.; Zheng, G.; Yan, Y.; Akram, R.; Uher, C.; Tang, X. High Thermoelectric Performance of Higher Manganese Silicides Prepared by Ultra-Fast Thermal Explosion. *J. Mater. Chem. C* **2015**, *3*, 12116−12122.
(46) Zhao, L.; Islam, S. M. K. N.; Wang, J.; Cortie, D. L.; Wang, X.; Cheng, Z.; Wang, J.; Ye, N.; Dou, S.; Shi, X.; Chen, L.; Snyder, G. J.; Wang, X. Significant Enhancement of Figure-of-Merit in Carbon-Reinforced Cu_2Se Nanocrystalline Solids. *Nano Energy* **2017**, *41*, 164−171.
(47) Delaire, O. Phonon Scattering in Thermoelectrics: Thermal Transport, Strong Anharmonicity, and Emergent Quasiparticles. *Bull. Am. Phys. Soc.* 2017, *62*.
(48) Hong, J.; Delaire, O. Electronic Instability and Anharmonicity in SnSe. 2016, arXiv:1604.07077. arXiv.org e-Print archive. https://arxiv.org/abs/1604.07077.
(49) Tang, G.; Liu, J.; Zhang, J.; Li, D.; Rara, K. H.; Xu, R.; Lu, W.; Liu, J.; Zhang, Y.; Feng, Z. Realizing High Thermoelectric Performance below Phase Transition Temperature in Polycrystalline SnSe *via* Lattice Anharmonicity Strengthening and Strain Engineering. *ACS Appl. Mater. Interfaces* **2018**, *10*, 30558−30565.
(50) Hong, M.; Chen, Z.-G.; Pei, Y.; Yang, L.; Zou, J. Limit of *ZT* Enhancement in Rocksalt Structured Chalcogenides by Band Convergence. *Phys. Rev. B* **2016**, *94*, 161201.
(51) Lv, H. Y.; Lu, W. J.; Shao, D. F.; Sun, Y. P. Enhanced Thermoelectric Performance of Phosphorene by Strain-Induced Band Convergence. *Phys. Rev. B* **2014**, *90*, No. 085433.
(52) Pei, Y.; Shi, X.; LaLonde, A.; Wang, H.; Chen, L.; Snyder, G. J. Convergence of Electronic Bands for High Performance Bulk Thermoelectrics. *Nature* **2011**, *473*, 66−69.
(53) Hong, M.; Chasapis, T. C.; Chen, Z.-G.; Yang, L.; Kanatzidis, M. G.; Snyder, G. J.; Zou, J. *n*-Type $Bi_2Te_{3-x}Se_x$ Nanoplates with Enhanced Thermoelectric Efficiency Driven by Wide-Frequency Phonon Scatterings and Synergistic Carrier Scatterings. *ACS Nano* **2016**, *10*, 4719−4727.
(54) Shi, X.; Wu, A.; Feng, T.; Zheng, K.; Liu, W.; Sun, Q.; Hong, M.; Pantelides, S. T.; Chen, Z.-G.; Zou, J. High Thermoelectric Performance in *p*-Type Polycrystalline Cd-Doped SnSe Achieved by a Combination of Cation Vacancies and Localized Lattice Engineering. *Adv. Energy Mater.* **2019**, DOI: 10.1002/aenm.201803242.

DOI: 10.1021/acsami.8b21699
ACS Appl. Mater. Interfaces 2019, 11, 8051−8059

Supporting Information

Super Large $Sn_{1-x}Se$ Single Crystals with Excellent Thermoelectric Performance

Min Jin[*,a,b,1], *Xiao-Lei Shi*[c,1], *Tianli Feng*[d,e], *Weidi Liu*[c], *Haifeng Feng*[f], *Sokrates T. Pantelides*[d,e], *Jun Jiang*[b], *Yunxia Chen*[a], *Yi Du*[f], *Jin Zou*[*,c,g], *and Zhi-Gang Chen*[*,h,c]

[a] College of Materials, Shanghai Dianji University, Shanghai 201306, P R China

[b] Ningbo Institute of Materials Technology and Engineering, Chinese Academy of Sciences, Ningbo 315201, P R China

[c] Materials Engineering, University of Queensland, Brisbane, QLD 4072, Australia

[d] Department of Physics and Astronomy and Department of Electrical Engineering and Computer Science, Vanderbilt University, Nashville, Tennessee 37235, USA

[e] Center for Nanophase Materials Sciences (CNMS), Oak Ridge National Laboratory, Oak Ridge, Tennessee 37831, USA

[f] Institute for Superconducting and Electronic Materials (ISEM), Australian Institute for Innovative Materials (AIIM), University of Wollongong, Wollongong, NSW 2500, Australia

[g] Centre for Microscopy and Microanalysis, University of Queensland, Brisbane, QLD 4072, Australia

[h] Centre for Future Materials, University of Southern Queensland, Springfield, QLD 4300, Australia

AUTHOR INFORMATION

[1] These authors contribute equally to this work.

Corresponding Author

* zhigang.chen@usq.edu.au (ZGC); zhigang.chen@uq.edu.au (ZGC)

* j.zou@uq.edu.au (JZ)

* jmaish@aliyun.com (MJ)

Section 1. Sn-Se binary phase diagrams.

Figure S1 is the Sn-Se binary phase diagrams. As can be seen, there are two stable SnSe phases, denoted as α-SnSe (low temperature) and β-SnSe (high temperature),[1] respectively. In order to obtain high pure and stable SnSe compounds, the synthesis temperature is to set as >1134 K, which is the melting point.[1] Meanwhile, to achieve off-stoichiometric SnSe single crystals, we choose the stoichiometric ratio of precursors Sn and Se as 0.98:1 (shown in **Figure S1**), and finally realize off-stoichiometric $Sn_{1-x}Se$ single crystals determined *via* intensive compositional characterizations.

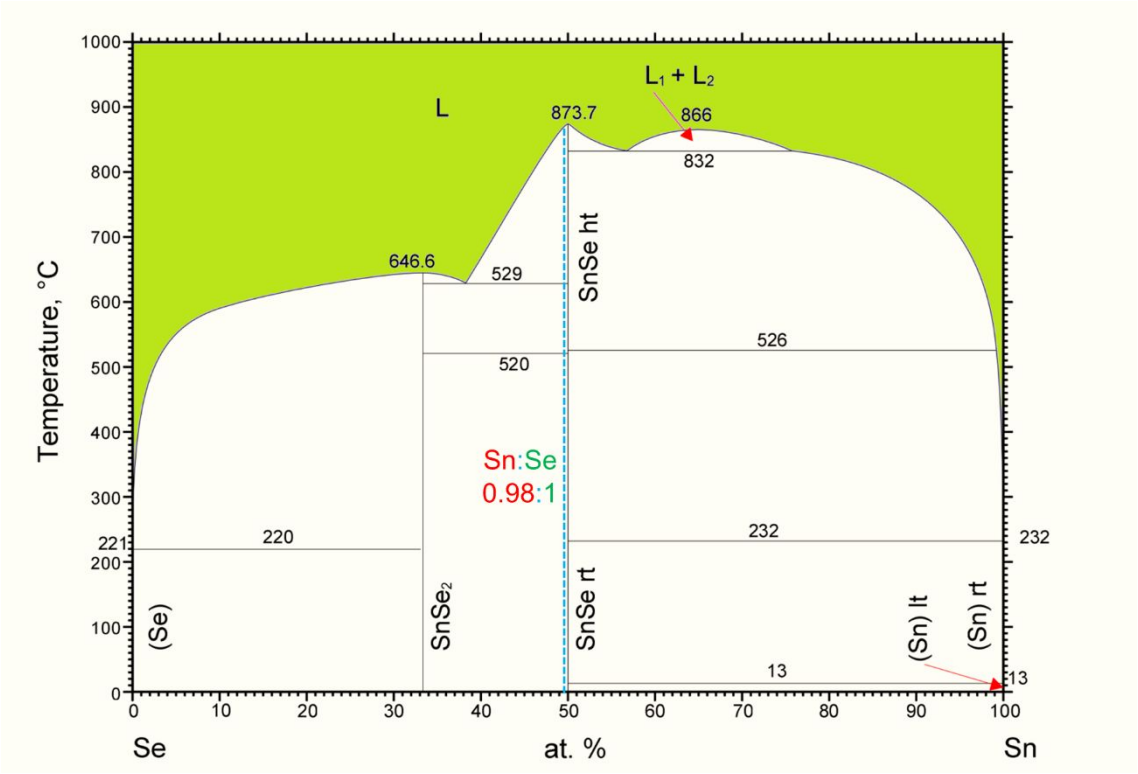

Figure S1. Sn-Se binary phase diagram. Reproduced and revised with permission. Copyright 2019, Springer Nature.[2]

Section 2. XRD and SEM results for our synthesized polycrystalline SnSe as precursors of followed single crystal growth.

Figure S2(a) shows XRD results for our synthesized polycrystalline SnSe as precursors of followed single crystal growth (both polycrystalline SnSe and $Sn_{1-x}Se$ powders). It is clearly seen that all diffraction peaks can be indexed as orthorhombic-structured SnSe with lattice parameters of a =1.14 nm, b = 0.42 nm and c = 0.44 nm and a space group of *Pnma*, according to the JCPDS 48-1224 Standard Identification Card. The strongest diffraction peaks of 400* suggest our products contain significant (100) surfaces.[1, 3-5] **Figure S2(b)** also shows the 111^* and 400^* peaks for both polycrystalline SnSe and $Sn_{1-x}Se$ powders. Compared with SnSe powders, all peaks from $Sn_{1-x}Se$ powders are deviated from the standard value at 2θ = 30.462° for 111^* and 31.081° for 400^*. The right-shifted diffraction peaks indicate a high Sn vacancy level in SnSe.[1, 4] **Figure S2(c)** is a SEM image of our synthesized polycrystalline $Sn_{1-x}Se$ powders. It is clear that these polycrystalline SnSe powders possess layered structure. The layers are (100) surfaces, and this is why the (400) peak is the most significant peak in the XRD results shown in **Figure 2(a)**.

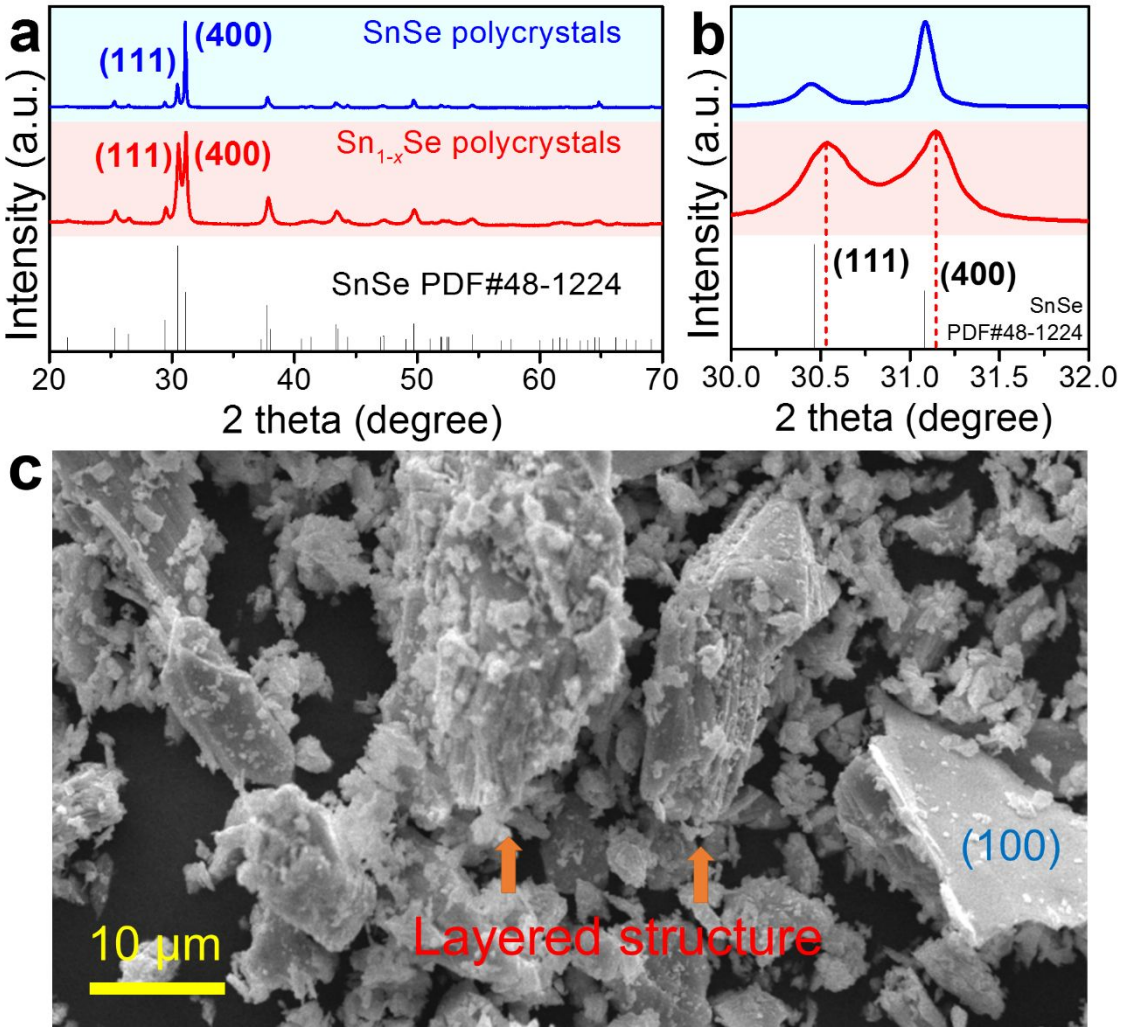

Figure S2. Additional morphological and structural characterizations of SnSe polycrystals. (a) X-ray diffraction (XRD) results for our synthesized polycrystalline SnSe and $Sn_{1-x}Se$ as precursors of followed single crystal growth; (b) enlarged 111* and 400* peaks to see the peak deviation of the polycrystalline SnSe and $Sn_{1-x}Se$; and (c) SEM image for our synthesized polycrystalline $Sn_{1-x}Se$ powders.

Section 3. TG results for our synthesized SnSe single crystals.

Figure S3 compares the thermogravimetric (TG) curves of SnSe and $Sn_{1-x}Se$. The pink dashed line at 800 K indicates the phase transition between α-SnSe and β-SnSe. It is obvious that the compositional difference can result in a different crystal volatilization. $Sn_{1-x}Se$ single crystals start to volatilize from 730 K, which is about 174 K lower than that of SnSe single crystals. Such phenomenon is mainly because of the excess Se in $Sn_{1-x}Se$ single crystals. For the convenience of comparison, the TG curves of Se and Sn elements are also illustrated in **Figure S3**. It is noticed Se is very easy to volatilize (start at 593 K), but the weight of Sn slightly increases as it reacts with residual oxygen in the chamber of equipment. The TG results indicate that the stable temperature range for measuring the thermoelectric performance is better to be controlled within 800 K.

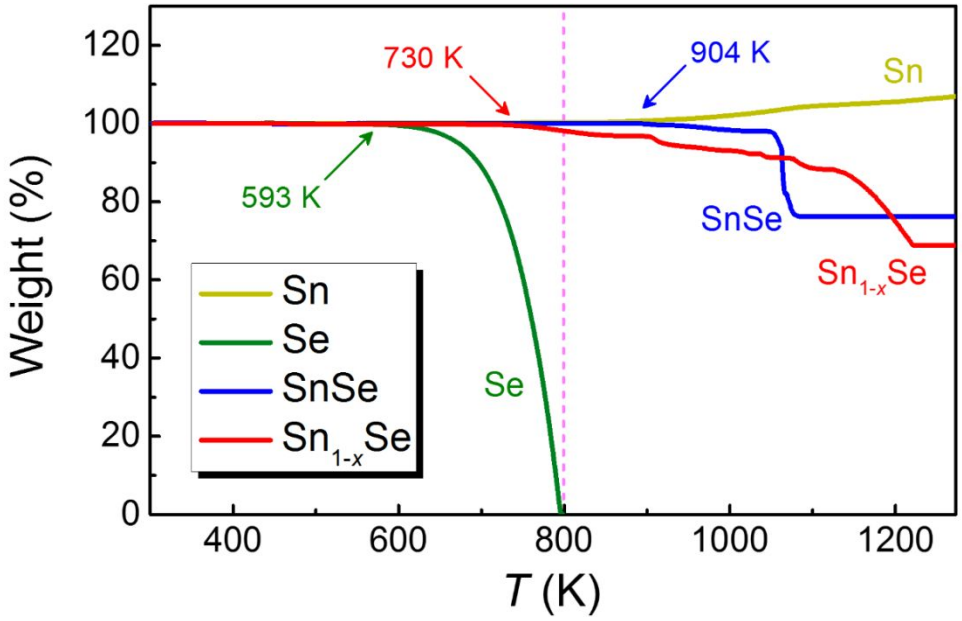

Figure S3. Thermogravimetric (TG) curves of Sn, Se, SnSe, and $Sn_{1-x}Se$. The pink dashed line at 800 K indicates the phase transition between α-SnSe and β-SnSe.

Section 4. Examination of the reproducibility for obtained thermoelectric properties.

For SnSe, the phase transition between α-SnSe and β-SnSe at 800 K is detrimental to the stability of performance, as well as the mechanical properties.[1] To evaluate the reproducibility of our thermoelectric properties, we tested 6 times for our $Sn_{1-x}Se$ single crystals from room temperature to 793 K. **Figure S4** shows the *T*-dependent properties (σ, S, $S^2\sigma$, κ, and ZT) with different measured times. All properties were measured along in-plane directions (*bc* axis). The 1st, 3rd and 5th measurements were taken under heating processes, and the other three measurements were taken under cooling processes. The results indicate that the reproducibility of our obtained thermoelectric properties are high under 793 K.

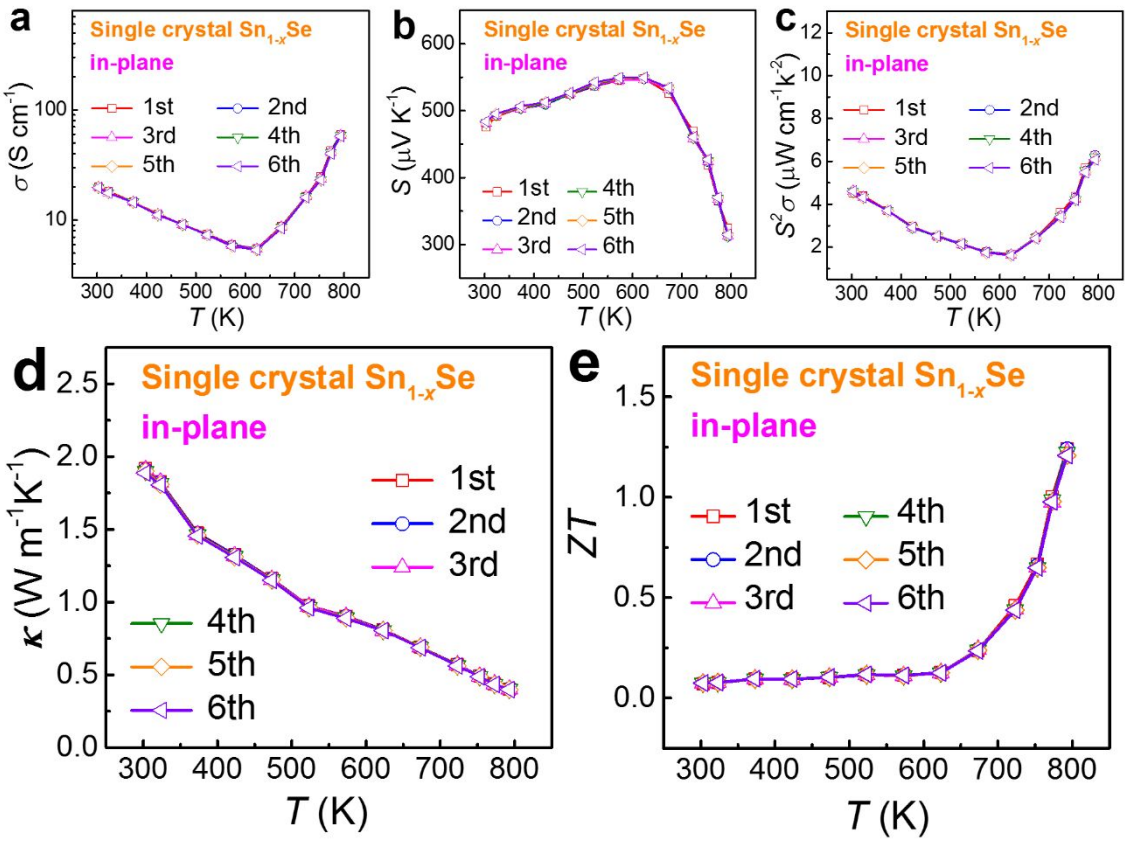

Figure S4. *T*-dependent properties with different measured times for our $Sn_{1-x}Se$ single crystals: (a) σ; (b) S; (c) $S^2\sigma$; (d) κ; and (e) ZT. All properties are measured along the in-plane direction. The 1st, 3rd and 5th measurements were taken under heating processes, and the other three measurements were taken under cooling processes.

Section 5. Anisotropy for the achieved thermoelectric performance of $Sn_{1-x}Se$ single crystals.

To demonstrate the anisotropy of thermoelectric performance in our $Sn_{1-x}Se$ single crystals, we show the plots of properties (temperature-dependent σ, S, $S^2\sigma$, p, μ, D, κ, and ZT) with different measured directions in **Figure S5**, in which label "in-plane" stands for the measured directions along the *bc*-axis and label "out-of-plane" represents the measured directions along the *a*-axis. It is clear that except S and p, all properties measured along the *bc*-axis are higher than that measured along the *a*-axis due to the anisotropy. This is why we chose *bc*-axis as the main measured direction in the main text.

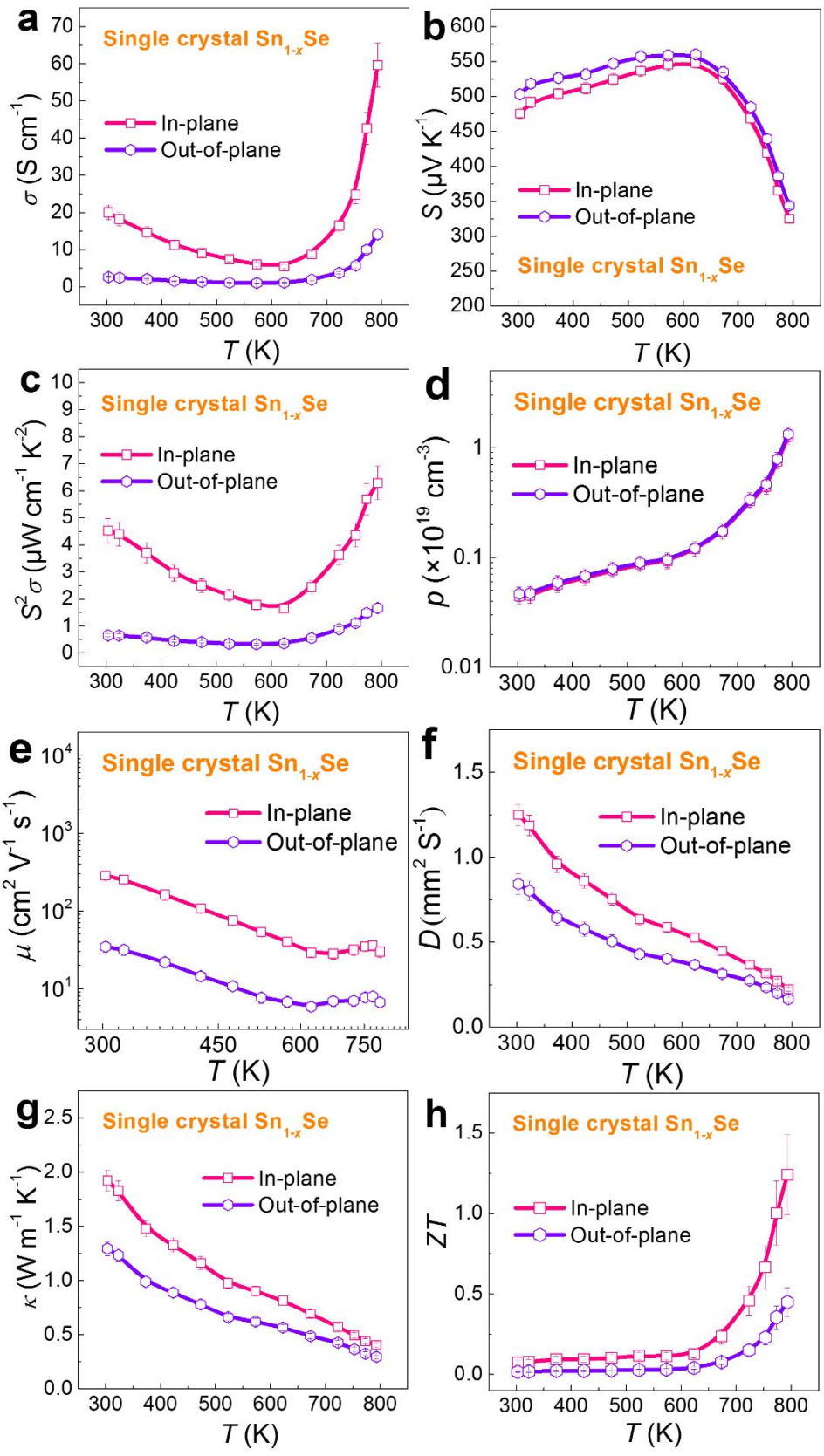
a
Single crystal Sn1-xSe
In-plane
Out-of-plane
σ (S cm-1)
T (K)
b
S (μV K-1)
c
S2σ (μW cm-1 K-2)
d
p (×1019 cm-3)
e
μ (cm2 V-1 s-1)
f
D (mm2 S-1)
g
κ (W m-1 K-1)
h
ZT

Figure S5. Plots of *T*-dependent properties with different measured directions from our $Sn_{1-x}Se$ single crystals: (a) σ; (b) S; (c) $S^2\sigma$; (d) p, (e) μ, (f) D, (g) κ, and (h) ZT. The label "in-plane" stands for the measured directions along the *bc*-axis and label "out-of-plane" represents the measured directions along the *a*-axis.

Section 6. Measured D and C_p for SnSe single crystals.

The measured thermal diffusivity (D) and specific heat (C_p) for our SnSe single crystals are shown in **Figure 6(a, b)**, respectively. The measured room temperature densities ρ are also shown in **Figure 6(a)**. The C_p are stable in the entire temperature range except a small peak at 800 K, indicating the phase transition between α-SnSe and β-SnSe. The difference between measured phase transition temperature (798.8 K for $Sn_{1-x}Se$) and theoretical temperature (800 K for SnSe) comes from the slight composition difference between $Sn_{1-x}Se$ and SnSe.

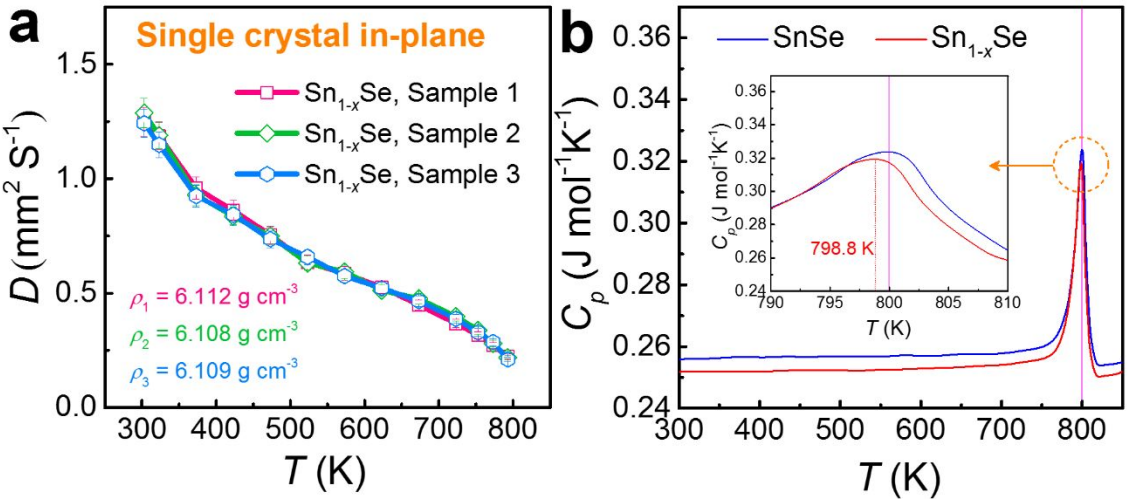

Figure S6. Measured thermal diffusivity D and specific heat C_p of our SnSe single crystals. (a) Plots of T-dependent D for $Sn_{1-x}Se$ single crystals with room temperature densities ρ; (b) T-dependent C_p for both SnSe and $Sn_{1-x}Se$ single crystals, the enlarged curves at ~800 K is shown in the inset. The pink line at 800 K indicates the phase transition between α-SnSe and β-SnSe.

Section 7. Calculated *m for $Sn_{1-x}Se$ single crystals with SPB model calculation details.**

The calculated average effective mass (*m**) for $Sn_{1-x}Se$ single crystals are shown in **Figure S7**. The *m** were calculated *via* a single parabolic band (SPB) model.[6-9] It is clear that the *m** are almost stable with increasing the temperature.

For calculation details, the the pertinent equations are as follows:

$$S(\eta) = \frac{k_B}{e} \cdot \left[\frac{\left(r + \frac{5}{2}\right) \cdot F_{r+\frac{3}{2}}(\eta)}{\left(r + \frac{3}{2}\right) \cdot F_{r+\frac{1}{2}}(\eta)} - \eta \right] \tag{S6-1}$$

$$n = \frac{1}{e \cdot R_H} = \frac{(2m^* \cdot k_B T)^{\frac{3}{2}}}{3\pi^2 \hbar^3} \cdot \frac{\left(r + \frac{3}{2}\right)^2 \cdot F^2_{r+\frac{1}{2}}(\eta)}{(2r + \frac{3}{2}) \cdot F_{2r+\frac{1}{2}}(\eta)} \tag{S6-2}$$

$$\mu = \left[\frac{e\pi\hbar^4 \quad C_l}{\sqrt{2}(k_B T)^{\frac{3}{2}} E_{def}{}^2 (m^*)^{\frac{5}{2}}} \right] \frac{(2r + \frac{3}{2}) \cdot F_{2r+\frac{1}{2}}(\eta)}{\left(r + \frac{3}{2}\right)^2 \cdot F_{r+\frac{1}{2}}(\eta)} \tag{S6-3}$$

$$L = \left(\frac{k_B}{e}\right)^2 \cdot \left\{ \frac{\left(r + \frac{7}{2}\right) \cdot F_{r+\frac{5}{2}}(\eta)}{\left(r + \frac{3}{2}\right) \cdot F_{r+\frac{1}{2}}(\eta)} - \left[\frac{\left(r + \frac{5}{2}\right) \cdot F_{r+\frac{3}{2}}(\eta)}{\left(r + \frac{3}{2}\right) \cdot F_{r+\frac{1}{2}}(\eta)} \right]^2 \right\} \tag{S6-4}$$

where η, k_B, e, r, R_H, $\hbar$, C_l, and E_{def} are the reduced Fermi level, the Boltzmann constant, the electron charge, the carrier scattering factor (r = -1/2 for acoustic phonon scattering), the Hall coefficient, the reduced plank constant, the elastic constant for longitudinal vibrations, and the deformation potential coefficient, respectively. Here:

$$C_l = v_l^2 \cdot \rho \quad \text{(S6-5)}$$

where v_l is the longitudinal sound velocity and taken as 2530 m·s^{-1} in this study.[10] $F_i(\eta)$ is the Fermi integral expressed as:

$$F_i(\eta) = \int_0^\infty \frac{x^i}{1 + e^{(x-\eta)}} dx \quad \text{(S6-6)}$$

The predicted hole carrier concentration p-dependent ZT values in **Figure 6(i)** are also calculated based on the above model at different temperature, and the κ_l used in the calculation are derived from **Figure 6(e)**.

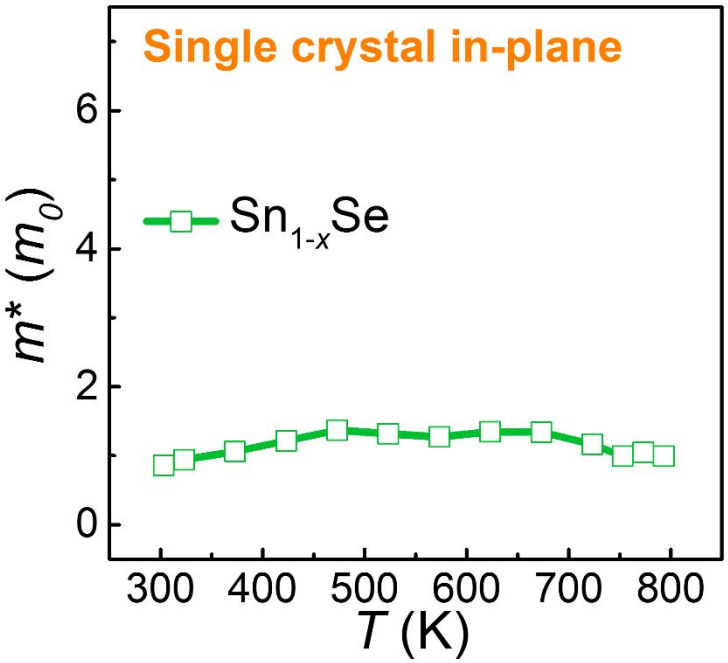

Figure S7. Calculated effective mass m*.

Section 8. Difference between the experimental and theoretical calculated *p* for $Sn_{1-x}Se$.

To evaluate the theoretical hole carrier concentration *p* with a high accuracy, we perform both first-principle calculations as well as common theoretical calculations to estimate the *p* value. The calculation is based on the formula shown as below:

$$p = \int_{-\infty}^{VBM} (1 - f) DOS(E) dE \quad \text{(S8-1)}$$

$$f = \frac{1}{1 + \exp\left(\frac{E - E_F}{k_B T}\right)} \quad \text{(S8-2)}$$

The calculated results *via* DFT with both supercells of 2×4×4 (256 atoms) and 2×5×5 (400 atoms) as well as common theoretical evaluation are shown in **Figure S8**. It is clear to see that the theoretical *p* value for the presence of ~0.3 % Sn vacancies in SnSe is calculated as ~1.13×10^{20} cm^{-3}. This value is higher than the experimental value of ~1.2×10^{19} cm^{-3}, approximately 1 order larger than experimental result. There are three reasons for the deviation of experimental data from calculated results, include the precision of experimentally achieved "*x*" value, the existence of Se vacancies in the SnSe matrix which is very common in selenides,[11-12] and the hydrogenation of Sn vacancies which is also common seen in selenides.[13-14] All of these reasons are hard to avoid, resulting in the difference between experimental and calculated values of *p*.

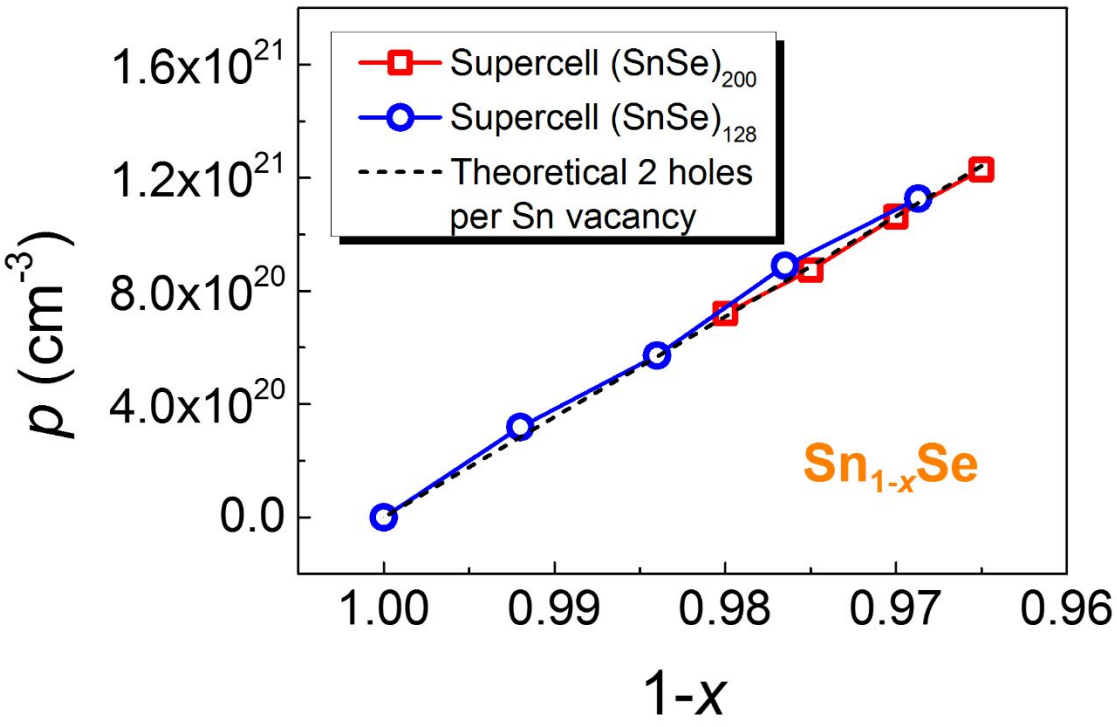

Figure S8. Theoretical calculated hole concentration p of Sn_xSe.

Reference

(1) Chen, Z.-G.; Shi, X.; Zhao, L.-D.; Zou, J. High-Performance SnSe Thermoelectric Materials: Progress and Future Challenge. *Prog. Mater. Sci.* **2018**, *97*, 283-346.

(2) Okamoto, H. Se-Sn (Selenium-Tin). *J. Phase. Equilib.* **1998**, *19*, 293.

(3) Shi, X. L.; Zheng, K.; Liu, W. D.; Wang, Y.; Yang, Y. Z.; Chen, Z. G.; Zou, J. Realizing High Thermoelectric Performance in *n* ‐ Type Highly Distorted Sb ‐ Doped SnSe Microplates *via* Tuning High Electron Concentration and Inducing Intensive Crystal Defects. *Adv. Energy Mater.* **2018**, *8*, 1800775.

(4) Shi, X.; Chen, Z.; Liu, W.; Yang, L.; Hong, M.; Moshwan, R.; Huang, L.; Zou, J. Achieving High Figure of Merit in *p*-Type Polycrystalline $Sn_{0.98}Se$ *via* Self-Doping and Anisotropy-Strengthening. *Energy Storage Mater.* **2018**, *10*, 130-138.

(5) Shi, X. L.; Zheng, K.; Hong, M.; Liu, W. D.; Moshwan, R.; Wang, Y.; Qu, X.-L.; Chen, Z. G.; Zou, J. Boosting the Thermoelectric Performance of *p*-Type Heavily Cu-Doped Polycrystalline SnSe *via* Inducing Intensive Crystal Imperfections and Defect Phonon Scattering. *Chem. Sci.* **2018**, *9*, 7376-7389.

(6) Xu, Y.; Li, W.; Wang, C.; Li, J.; Chen, Z.; Lin, S.; Chen, Y.; Pei, Y. Performance Optimization and Single Parabolic Band Behavior of Thermoelectric MnTe. *J. Mater. Chem. A* **2017**, *5*, 19143-19150.

(7) Shen, J.; Chen, Z.; lin, S.; Zheng, L.; Li, W.; Pei, Y. Single Parabolic Band Behavior of Thermoelectric *p*-Type $CuGaTe_2$. *J. Mater. Chem. C* **2016**, *4*, 209-214.

(8) She, X.; Su, X.; Du, H.; Liang, T.; Zheng, G.; Yan, Y.; Akram, R.; Uher, C.; Tang, X. High Thermoelectric Performance of Higher Manganese Silicides Prepared by Ultra-Fast Thermal Explosion. *J. Mater. Chem. C* **2015**, *3*, 12116-12122.

(9) Zhao, L.; Islam, S. M. K. N.; Wang, J.; Cortie, D. L.; Wang, X.; Cheng, Z.; Wang, J.; Ye, N.; Dou, S.; Shi, X.; Chen, L.; Snyder, G. J.; Wang, X. Significant Enhancement of Figure-of-Merit in Carbon-Reinforced Cu_2Se Nanocrystalline Solids. *Nano Energy* **2017**, *41*, 164-171.

(10) Xiao, Y.; Chang, C.; Pei, Y.; Wu, D.; Peng, K.; Zhou, X.; Gong, S.; He, J.; Zhang, Y.; Zeng, Z.; Zhao, L.-D. Origin of Low Thermal Conductivity in SnSe. *Phys. Rev. B* **2016**, *94*, 125203.

(11) Li, Q.; Zhang, L.; Yin, J.; Sheng, Z.; Chu, X.; Wang, F.; Zhu, F. Study on the Thermoelectric Performance of Polycrystal SnSe with Se Vacancies. *J. Alloy. Compd.* **2018**, *745*, 513-518.

(12) Han, G.; Chen, Z. G.; Drennan, J.; Zou, J. Indium Selenides: Structural Characteristics, Synthesis and their Thermoelectric Performances. *Small* **2014**, *10*, 2747-2765.

(13) Varley, J.; Peelaers, H.; Janotti, A.; Van de Walle, C. Hydrogenated Cation Vacancies in Semiconducting Oxides. *J. Phys. Condens. Mat.* **2011**, *23*, 334212.

(14) Delbecq, F.; Sautet, P. Influence of Sn Additives on the Selectivity of Hydrogenation of α-β-Unsaturated Aldehydes with Pt Catalysts: A Density Functional Study of Molecular Adsorption. *J. Catal.* **2003**, *220*, 115-126.